



Optimizing thermal stability and mechanical behavior in segregation-engineered nanocrystalline Al–Ni–Ce alloys: A combinatorial study

Jungho Shin^{1,2}, Fulin Wang^{1,3}, Glenn H. Balbus¹, Tianjiao Lei⁴, Timothy J. Rupert⁴, Daniel S. Gianola^{1,a)} 

¹Materials Department, University of California, Santa Barbara, CA 93106, USA

²Gangneung-Wonju National University, Gangneung-si, Gangwon-do, Republic of Korea

³National Engineering Research Center of Light Alloy Net Forming, School of Materials Science and Engineering, Shanghai Jiao Tong University, Shanghai, China

⁴Department of Materials Science and Engineering, University of California, Irvine, CA 92697, USA

^{a)}Address all correspondence to this author. e-mail: gianola@ucsb.edu

Received: 13 April 2022; accepted: 23 August 2022; published online: 8 September 2022

The deliberate use of solute enrichment at grain boundaries, otherwise known as segregation engineering, is a promising approach to tailor the properties of interface-dominated materials such as nanocrystalline alloys. The ensuing chemical and structural evolution at grain boundaries can give rise to thermal stability and excellent mechanical properties, but the interplay between enrichment, phase decomposition, grain growth, and mechanical behavior exists in a vast composition and processing space. In this study, a combinatorial synthesis and rapid characterization approach was applied to segregation-engineered nanocrystalline Al–Ni–Ce alloys to assess the evolution of microstructure and resulting mechanical behavior as functions of alloying content and annealing conditions. In addition to the identification of alloys and processing conditions that give rise to exceptional thermal stability, strength retention, and homogeneous plastic flow, we construct combined thermal stability and deformation mechanism maps that demarcate several important regimes of behavior.

Introduction

A prevailing engineering strategy for the design of advanced high-strength structural materials has been to introduce a high density of interfaces, such as grain boundaries (GBs) in nanocrystalline (NC) metals and alloys. Decorating the GB with alloying elements mitigates their inherently poor thermal stability [1, 2]. However, circumventing the tradeoff between thermal stability, strength, and damage tolerance in NC alloys has been a primary challenge in the field. Finding a balanced suite of these properties is a current bottleneck for widespread technological adoption. While the vast majority of work has focused on elemental and binary NC alloys [3–12], increasingly compelling evidence suggests that complex solute segregation in multi-component systems (ternary and higher) promotes higher performance [13–16]. In some cases, with judicious selection of alloying species and processing pathways, unique GB states such as amorphous intergranular films (AIF), otherwise known as

amorphous complexions, have been reported [17–19]. Hosting such disordered GBs in Al-based NC alloys gives rise to exceptional thermal stability and mechanical behavior [20, 21], and also contributes to efficient densification of bulk NC alloys by powder metallurgy routes [2]. However, an understanding of the complex interplay between segregation, microstructural evolution, and resulting thermal stability and mechanical behavior in the vast compositional space remains elusive.

Segregation engineering significantly enhances the thermal stability of NC alloys [22–24] by either reducing the driving force (via lowering of the interfacial excess energy) for grain growth [11, 24–28] or by reducing the mobility (via hindering atomic motion) for migration of GBs [10, 29–33], or by some combination of the two depending on the choice of the constituent elements. In both cases, the alloy design space widens as the GB region becomes itself a feature to be tailored in tandem with the host matrix material [2, 34]. Despite being a barrier to

grain growth, solute enriched GBs often compete with phase separation at elevated temperatures, leading to grain coarsening and deterioration of mechanical strength after nucleating second phases. Chemically enriched AIFs can host a range of structural and chemical order as well as a variety of thicknesses within a polycrystalline GB network [34, 35], all of which presumably influences thermal stability, potential phase decomposition, and concomitant mechanical behavior in NC alloys [20, 21, 36]. Elucidating the underlying mechanisms for microstructural evolution, along with the temperature ranges over which GBs are compositionally enriched and where phase separation may occur, involves interrogation over both composition and processing space. However, meticulous experimental characterization is typically required to correlate evolving structure and properties and is usually accomplished for a limited composition range [37–39].

Accordingly, higher throughput approaches to map regimes in compositional space promise to accelerate the discovery of an optimized suite of properties in segregation-engineered NC alloys, and may enable predictive capability for the retention of the beneficial properties at service temperatures. Combinatorial synthesis combined with rapid structure–property mapping of segregation-engineered NC alloys is an emerging approach to address compositional optimization, with successful demonstrations using thin-film approaches as applied to various properties of interest (mechanical [40, 41], electrical [42–44], optical [45], magnetic [46, 47], and corrosion [48]) and several materials classes (bulk metallic glasses [49–51], multi-principal element alloys (MPEA) [52–55]). The majority of combinatorial studies to date on NC alloys have focused on thermal stability and microstructural evolution. For instance, Kube et al. applied a combinatorial approach to identify thermal stability regimes in ternary Pt-rich NC alloys, where the influence of multiple segregating species was highlighted [56]. Li et al. reported links between GB segregation and phase decomposition in combinatorially synthesized NC CrCoNi alloys [57].

Here, we systematically vary the alloying content in a ternary NC Al–Ni–Ce system to examine the evolution of microstructure and resulting mechanical behavior in AIF-hosting alloys via synergistic co-segregation of alloying species to the GBs. The Al–Ni–Ce system is known to have good glass formability and high specific strength [58], and when produced in AIF-containing NC form, recently has been demonstrated to possess exceptional high-temperature stability and strength [21] as well as the suppression of shear localization [20]. We use a high throughput approach to assess the interplay between the degree of chemical segregation, grain growth, the evolution of strength following thermal exposure, phase separation, and the propensity to shear localization. We monitored the microstructure and hardness of combinatorially synthesized NC Al–Ni–Ce

alloys after exposure to various annealing temperatures. While no grain growth was measured in any of the examined alloys (3.1 at.% to 7.8 at.% of Ni + Ce) when annealing to above 60% of the melting temperature (T_m) of Al, a pronounced anneal hardening (+30% increase in hardness) was observed in alloys with concentrations above 6.8 at.% of Ni + Ce. With the aid of thermodynamic and kinetic stabilization owing to segregated grain boundaries, these higher compositions demonstrated excellent strength retention, exhibiting higher hardness values than the initial state despite the presence of second phases after being annealed at $0.7T_m$. The transition temperature to shear localization behavior increased with increased alloying content, and a longer annealing time alleviated the detrimental shear localization without significantly compromising strength. Finally, we generate a stability and mechanism map with four characteristic regions in composition-temperature space, which guides compositional tuning and heat treatments to optimize NC Al–Ni–Ce alloys.

Results

Combinatorial approach

We used two approaches to synthesizing combinatorial materials libraries in the present work. To generate libraries of Al-rich NC alloys, two targets (pure Al and $\text{Al}_{87}\text{Ni}_7\text{Ce}_6$) were co-sputtered with the targets pointing at the center of the substrate in confocal configuration. In the first approach (preliminary screening), deposition over a pre-patterned mask yielded 30 compositionally isolated NC alloys in a single sputtering cycle with spatially varying compositions owing to the natural overlap of the vapor from the two sources [Fig. 1(a)]. In the second approach used for targeted annealing studies, a compositional library was generated by synthesizing multiple samples in the form of discrete patches, each with uniform composition, by independently controlling the deposition rates of each target [Fig. 2(a)]. Multiple samples were deposited on a single {100} Si substrate by using a combination of a Cu mask with a 5 mm aperture and automated substrate translation. Six different compositions ranging from Ni + Ce = 3.1 at.% to 7.8 at.% were sputtered [Fig. 2(b)], followed by annealing in vacuum for 2 h and nanoindentation after each heating cycle.

In both approaches, the individual patch dimension (5 mm × 10 mm) allowed rapid probing of the structure and mechanical properties by semi-automated X-ray Diffraction (XRD), energy dispersive spectroscopy (EDS) in a scanning electron microscope (SEM), and nanoindentation. Compositional uniformity within each patch was high, with the variance in composition below the measurement uncertainty of 0.2 at.%. The XRD analysis confirmed that all the as-deposited alloys are single-phase face-centered cubic (FCC) and exhibit {111}

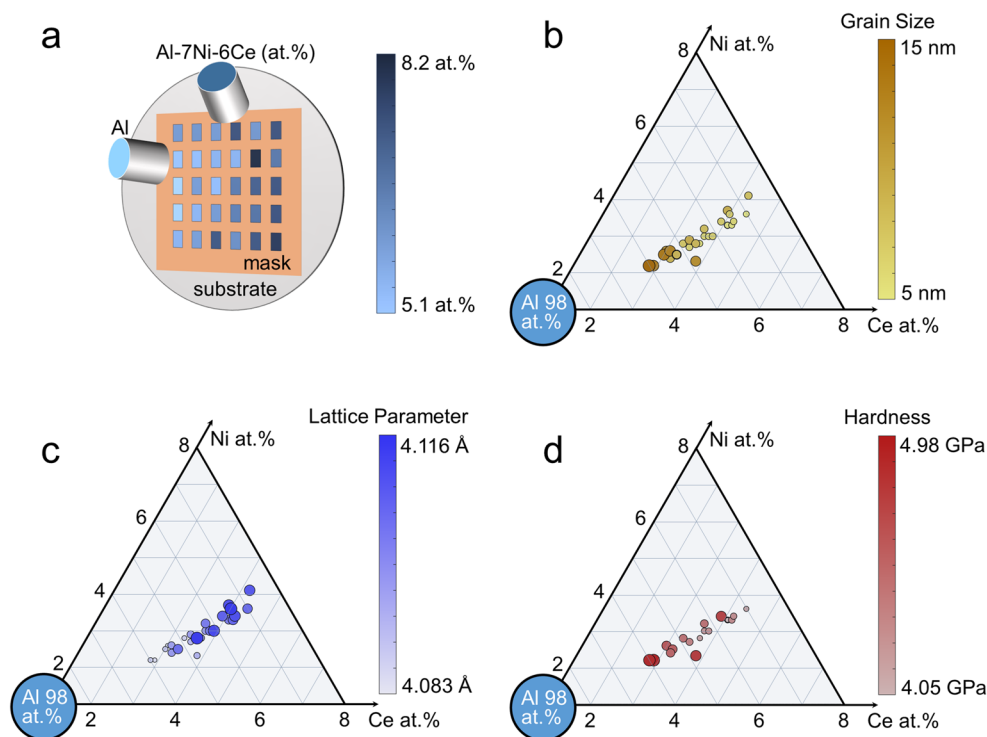


Figure 1: (a) Schematic of a compositional screening method using an arrayed mask on a substrate. (b) XRD measured grain size of the isolated film array; (c) XRD measured lattice parameters; and (d) Indentation hardness of the film array. In (b), (c), and (d), the size of the data markers are scaled to be proportional to their value.

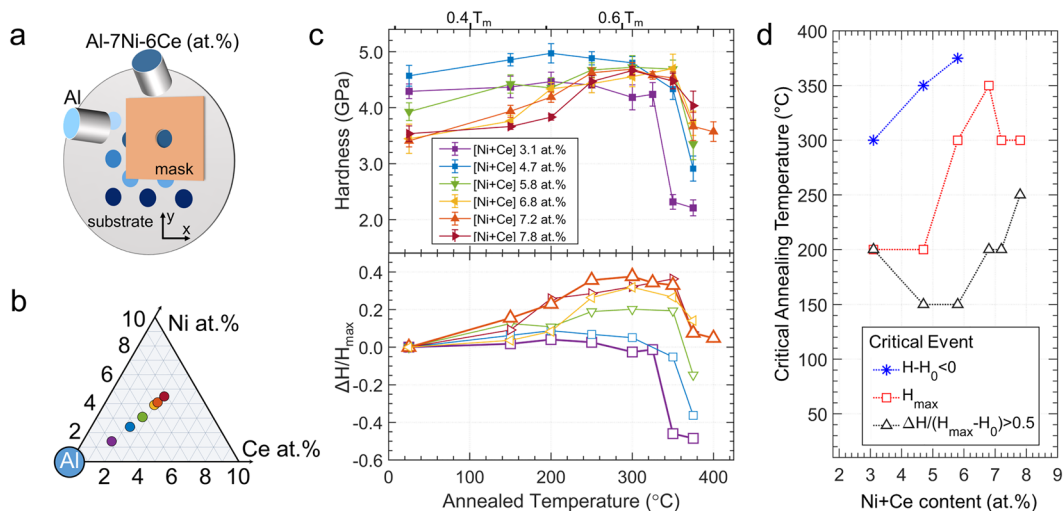


Figure 2: (a) Sputtering configuration using a cooled mask, stage motion, and actively controlled targets. (b) Composition map of alloys sputtered by active control of deposition powers. (c) Indentation hardness and the normalized hardness as a function of annealed temperatures. (d) Representative transition temperatures depicted by critical annealing temperatures as a function of alloying contents. ΔH is $H-H_0$, where H_0 is the hardness of each as-deposited film.

texture along the growth direction, which is typical for FCC thin films [59]. The combinatorial libraries were synthesized with a nominally constant Ni:Ce ratio of 1:1 as demonstrated in the

subsequent ternary plots (Fig. 1); thus, the cumulative atomic percentage of Ni + Ce is used to describe the alloying content throughout this article.

Initial compositional screening

The initial screening and rapid characterization exercise demonstrate how the Ni + Ce alloying additions profoundly affect the microstructure and the mechanical strength of the as-deposited films. Specifically, in the range of 5.1 at.% to 8.2 at.% global Ni + Ce content, the grain size, lattice parameter, and hardness are strong functions of the alloying content. The average grain size (d) of the as-deposited sputtered alloys ranges from 5 to 15 nm [Fig. 1(b)], a similar range that has been reported in other Al-based NC alloys [21, 60–62]. The films with higher alloying content tended to have smaller grain sizes, which can be ascribed to the hindrance of grain coalescence and subsequent growth during the deposition process owing to the presence of solute atoms [63, 64]. The lattice parameter (a) in the deposited alloys ranges from 4.08 to 4.12 Å [Fig. 1(c)], all exceeding that of elemental Al ($a_{\text{Al}} = 4.05$ Å). The lattice parameter of as-deposited films increases as the alloying content increases, which qualitatively follows the trend predicted from Vegard’s law as applied to the measured compositions of Ni and Ce in the Al matrix. All compositions investigated in this work exceed the maximum solubility of Ni and Ce in pure

Al in equilibrium, which are 0.11 at.% [65] and 0.01 at.% [66], respectively. While the indentation hardness of all of the as-deposited NC alloys exhibited very high values in the range of 4 GPa to 5 GPa [Fig. 1(d)], the hardness decreases as the grain size decreases. Thus, the as-deposited films ($d < 15$ nm) reflect the well-known breakdown from classical Hall–Petch behavior [67, 68], where GB-mediated plasticity dominates at grain sizes under ~ 20 nm [69–73]. Notably, a relatively small increase in alloying content (+ 3.1 at.%) resulted in a 66% decrease in the average grain size, 0.8% increase in the lattice parameter, and 19% decrease in hardness.

Hardness evolution

With initial trends identifying the strong role of Ni + Ce alloying content on microstructure and hardness, we further investigated the influence of composition on the thermal stability of the microstructure and retention of mechanical strength in targeted alloys. This was achieved by synthesizing multiple samples in the form of discrete patches, each with uniform composition, using the second approach described in the experimental methods

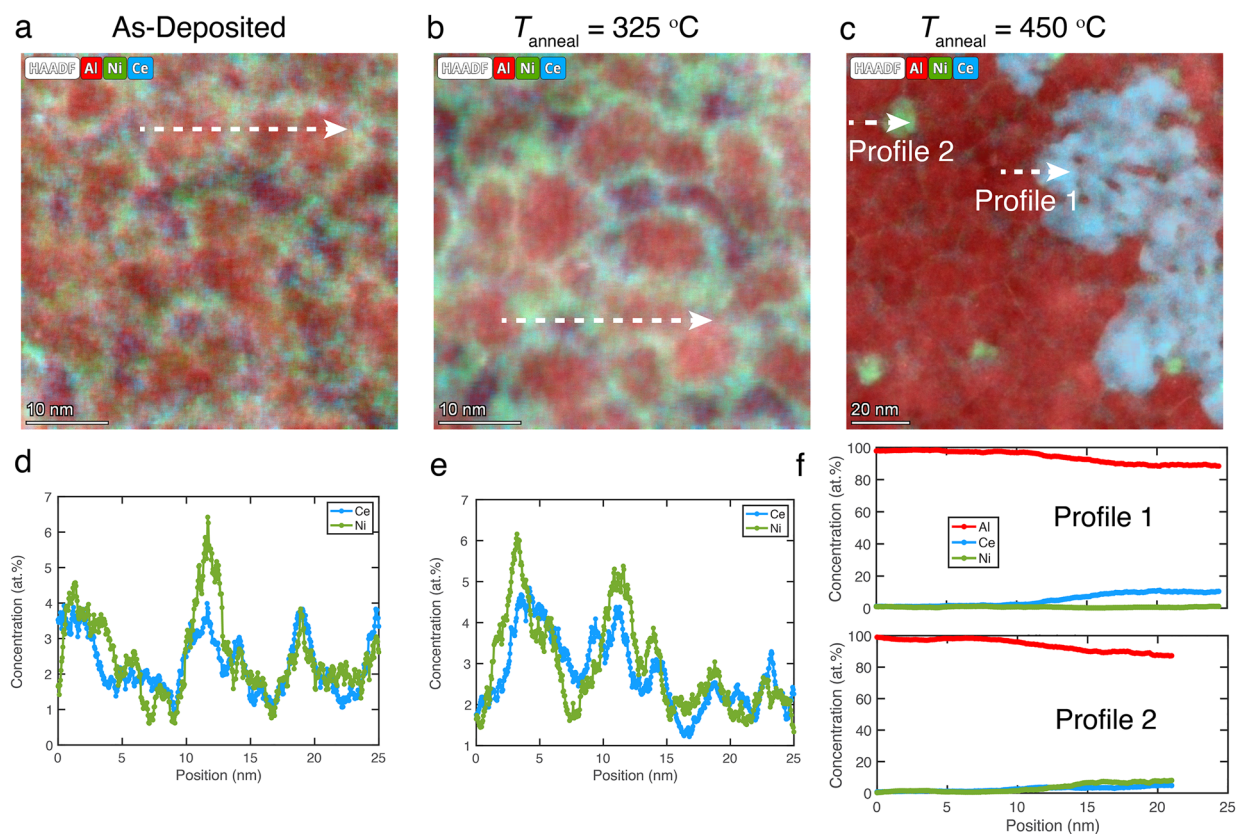


Figure 3: Evidence of co-segregation of Ni and Ce solutes to grain boundaries using scanning transmission electron microscopy (STEM)-EDS mapping in a representative alloy (5.1 at.% Ni + Ce content alloy, representing the compositional mid-point of the combinatorial study). Composite STEM-EDS elemental maps of Al, Ni, and Ce in the (a) as-deposited state, (b) following annealing at 325 °C, and (c) following annealing at 450 °C. (d–f) Compositional profiles corresponding to the dashed lines in (a–c) quantifying the co-segregation behavior and evolution upon annealing, as well as (f) the formation of two different intermetallic compounds when annealed at elevated temperatures (see text for detail).

section. Six different compositions ranging from Ni + Ce = 3.1 at.% to 7.8 at.% were sputtered [Fig. 2(b)], followed by annealing in vacuum for 2 h and nanoindentation after each heating cycle. Given the potent effects of dilute solute compositions identified in the preliminary screening, as well as the desire to limit the total alloying content while retaining good properties, we extended the compositional range downward for the secondary screening (which includes the annealing studies). We confirmed the co-segregation behavior of Ni and Ce solutes to grain boundaries using STEM-EDS elemental mapping, both in the as-deposited and annealed states, in a representative alloy with 5.1 at.% Ni + Ce content, which is approximately the compositional mid-point of the combinatorial study (Fig. 3). Compositional line profiles in the as-deposited [Fig. 3(d)] and following annealing to 325 °C [Fig. 3(e)] indicate that Ni and Ce solutes are co-located at grain boundaries, with more uniform enrichment following intermediate annealing treatments. At elevated temperatures [450 °C shown in Fig. 3(c) and (f)], intermetallic phases form, as discussed in detail later.

In the as-deposited films, the hardness is higher at leaner compositions [Fig. 2(c)], consistent with the previous observations [Fig. 1(d)]. The change of hardness upon thermal annealing was dependent on both the alloying content and the exposure temperatures; accordingly, we categorize two general regimes: (1) the anneal-hardening regimes (annealing < 375 °C), and (2) the anneal-softening regimes (annealing > 375 °C). The hardening behavior upon annealing among the material library is captured in the normalized change of hardness ($\Delta H/H_0$), where the change in hardness (ΔH) is defined with respect to the initial as-deposited hardness (H_0). The addition of alloying content increased the extent of anneal hardening and gradually increased the annealing temperature corresponding to the maximum hardness. In the anneal-hardening regime, the 3.1 at.% and 4.7 at.% compositions maintained their high strength without experiencing appreciable anneal hardening followed by the hardness only dropping below the initial value after annealing at 300 °C and 325 °C, respectively. On the other hand, pronounced anneal hardening, a distinct increase in hardness that peaks at around 300 °C, was observed at higher alloy contents. For instance, a composition of 5.8 at.% showed a 20% increase in hardness and retained these high values up to 350 °C, followed by a hardness loss at 375 °C. At higher alloying contents of 6.8 at.%, 7.2 at.%, and 7.8 at.%, a surprising increase in hardness of more than 30% was measured in the anneal-hardening regime. This increase of hardness upon annealing can be attributed to the GBs being stabilized by structural relaxation and segregation [73, 74]. As the grain size decreases, dislocation–GB interactions play an increasingly important role compared to intragranular dislocation activities, as evidenced by the observed changes of hardness. Thermal annealing can drive GB relaxation [75, 76] and segregation of

solute atoms [23, 24, 77] to impede dislocation–GB-mediated mechanisms; as a consequence, anneal hardening was more pronounced in the alloys with higher Ni + Ce content. The hardness retention of these higher alloying contents near $0.7T_m$ is noteworthy [78]. The hardness values after annealing at 375 °C exhibit measurable drops but remain above their initial values. The ranking of hardness values after annealing at 375 °C follows the level of Ni + Ce content in the alloys, with higher hardness for increasing alloying content, which is nearly the opposite trend of those in the as-deposited state. This suggests that the anneal-hardening regime reflects a substantial evolution in the GB chemistry and structure from the initial non-equilibrium as-deposited material.

These results allow for the identification of three representative transition temperatures [Fig. 2(d)]. First, there is a composition and temperature threshold for retaining strength above the as-deposited state following annealing, which is represented as $H - H_0 < 0$ (blue asterisks). The alloys leaner in Ni and Ce (3.1 at.%, 4.7 at.%, and 5.8 at.% compositions) lose their strength below that of the initial value following the anneal-hardening regime. Second, the temperature corresponding to the maximum hardness (H_{max} , red squares) sharply rose upon increasing the Ni + Ce level from 4.7 to 6.8 at.%, which suggests that additional thermal energy is needed to drive segregation and/or structural relaxation of the GBs as the solutes compete for sites in the GB. The H_{max} temperature slightly decreases in the last two compositions presumably due to the abundance of solutes near the GBs. Third, the onset and potency of anneal hardening can be captured by a temperature where the hardness increases by more than half of the peak value, defined as $\Delta H/(H_{max} - H_0) > 0.5$ (black triangles). A larger gap between the second and the third transition temperature indicates that the alloy readily hardens at lower temperatures and then gradually strengthens to the peak; a smaller gap indicates more rapid hardening after annealing at a critical temperature. Collectively, these temperature metrics for the anneal-hardening regime reflect the compositional dependence of the resulting GB enrichment and its influence on microstructural evolution and resulting strength retention.

The total alloying content predominates as the key design parameter that determines the initial microstructure, hardness, and the transition of mechanical strength upon annealing. As a whole, these alloys exhibited two characteristic behaviors in the evolution of hardness: (i) retention of high strength followed by a precipitous drop beyond $0.67T_m$ (Ni + Ce < 5.8 at.%), and (ii) pronounced anneal hardening with a less prominent drop leading to retention of the anneal-hardened state above the initial state (Ni + Ce > 5.8 at.%). This analysis thereby leads us to focus on Ni + Ce = 3.1 at.% and 7.2 at.% as two bounding cases to examine the evolution of microstructural features, i.e., lattice

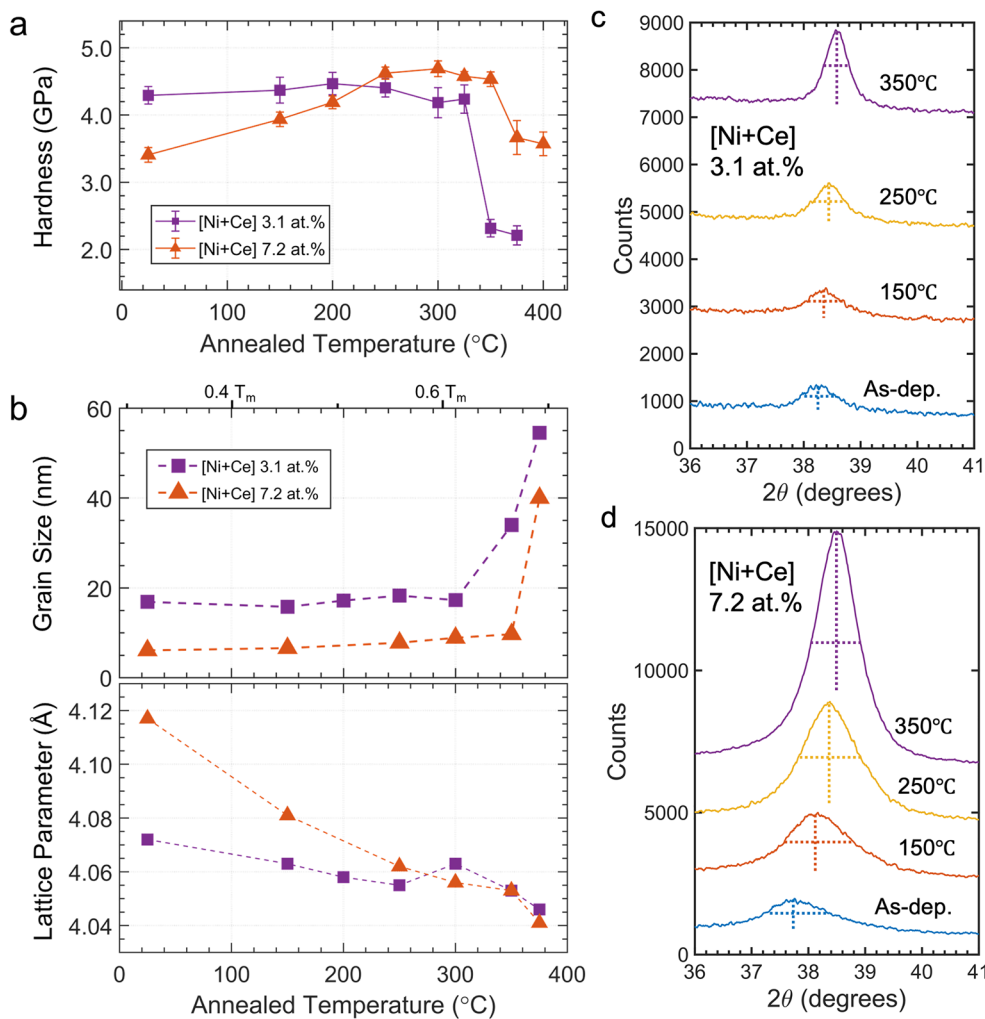


Figure 4: (a) Indentation hardness as a function of annealed temperatures and (b) Evolution of XRD measured grain size and lattice parameter of alloys with 3.1 at.% and 7.2 at.% Ni + Ce content. Evolution of the XRD profiles for the indexed {111} FCC peak for the (c) 3.1 at.% and (d) 7.2 at.% Ni + Ce content alloys after annealing at each temperature (listed next to each profile) for 2 h. The dashed lines are guides to the eye for peak positions widths.

parameter, grain size, secondary phases, and the tendency for shear localization.

Evolution of lattice parameters and grain sizes

We first correlate the evolution of hardness in these two model compositions [Fig. 4(a)] to those of the lattice parameter and grain size [Fig. 4(b)], with accompanying representative XRD profiles of the {111} FCC peak as a function of annealing temperature shown in Fig. 4(c, d)] in the regime where the nanocrystalline microstructure is stable. At annealing temperatures of 300 °C (~0.62 T_m) and below, the anneal-hardening behavior is linked to a decrease in the lattice parameters despite the grain sizes remaining unchanged in all samples. Over these temperatures marked by NC stability, the hardness of the leaner composition (3.1 at.%) marginally increased by 6.7% from 4.19 to 4.47 GPa, while the lattice parameter decreased 0.4% from

4.072 to 4.055 Å. In the higher composition sample (7.2 at.%), the hardness increased 38% from 3.41 to 4.69 GPa as the lattice parameter decreased by about 1.5% from 4.117 to 4.056 Å. Comparing the two compositions, a 5.7-fold increase of the accessible anneal-hardening potency corresponded to a fourfold increase in the lattice parameter change.

Increasing the alloying content lowered the initial strength in concert with a larger lattice parameter; however, the thermal annealing initiated a strong hardening behavior with a sharp decrease of the lattice parameter. Such a strong anneal-hardening response with stable grain sizes, in turn, leads to a final hardness of the 7.2 at.% alloy that surpasses that of the 3.1 at.% alloy after annealing to temperatures above 250 °C, at which their lattice parameters converge. Critically, the grain size remains constant up to 300 °C in both alloys, suggesting enrichment of Ni and Ce solutes in the GBs that enhances stability. The evolution of the lattice parameter indicates that the solutes that

initially partially reside in the grain interior segregate to the GB (since these regions do not contribute to X-ray peak broadening). While our results of GB chemical enrichment leading to the anneal-hardening behavior are consistent with other reports [74, 79], our compositional screening shows that the potency of this effect and the temperature range over which it is observed strongly depends on GB composition.

Both compositions exhibiting stable NC structures demonstrate a link between the evolution of lattice parameter—reflecting chemical and, presumably, structural transitions within the NC GB regions—and mechanical response. In this grain size regime, our results are consistent with emerging literature showing how the presence of solutes or solutal clusters at GBs can substantially strengthen the alloy [80, 81], even for fixed grain sizes [73, 80]. The lattice parameter of FCC Ni (3.524 Å) is smaller, while FCC Ce (5.162 Å) is larger than Al (4.050 Å). The initial lattice parameter of the 7.2 at.% alloy being larger than the 3.1 at.% alloy corroborates the initial screening results that confirm that more alloying content leads to larger lattice parameters (Fig. 1). Assuming Vegard's law for a fully saturated solid solution and a simple additive chemical strain from the Ni and Ce solutes, the predicted lattice parameters of the fully saturated state of 3.1 at.% (1.4 at.% Ni-1.7 at.% Ce) and 7.2 at.% (4.1 at.% Ni-3.1 at.% Ce) alloys would be 4.061 Å and 4.063 Å, respectively. For the as-deposited states, both measured values are in excess of these predictions, suggesting full enrichment of Ni at GBs and a super-saturated solid solution of Ce typical of the non-equilibrium sputtering process. These lattice parameter values also agree well with those previously observed during detailed TEM characterization of a nanocrystalline Al–Ni–Ce alloy [20, 21], as well as the chemical segregation during annealing. Apart from the chemical strain effect, residual stresses arising from the sputtering process can also influence the lattice parameter, as they would lead to XRD peak shifts. Sputtered metallic films are reported to experience in-plane biaxial compressive associated with typical growth conditions such as coefficient of thermal expansion mismatch and lattice mismatch. For instance, sputtered Al films on Si substrate can reach compressive stresses as high as 1 GPa depending on the sputtering parameters [82]. We expect that these origins of residual stress are minimal in the alloys produced in the present study owing to (i) low sputtering temperatures, (ii) the presence of a native amorphous layer on the substrates precluding epitaxial growth, and (iii) the growth of relatively thick films (~1 μm). However, intrinsic residual growth stresses arising from the nucleation of crystalline seeds, and their coalescence and growth, can also develop during thin-film deposition [64]. Indeed, the Poisson effect by a possible in-plane biaxial compressive residual stress can contribute to the measured lattice parameter via the interplanar spacing of {111} planes parallel to the growth substrates. Excluding the chemical strain effect from the alloying

and assuming an elastically isotropic pure Al film, we estimate an upper bound for the initial residual in-plane biaxial compressive stress of 129 MPa and 385 MPa for as-deposited 3.1 at.% and 7.2 at.% alloys, respectively. We conducted measurements of the in-plane biaxial residual stresses in these films using the $\sin^2\psi$ method [83] to estimate their magnitude, with the compressive stress released following low-temperature anneals. Nevertheless, we can still assess the influence of the existence of such an in-plane biaxial compressive residual stress, as it would lead to the underestimation of the true contact area (A_c) at a given indentation depth and, thus, a possible overestimation of hardness ($H = F/A_c$) [84–86]. Corrections for the true A_c would yield a higher slope in the hardness vs. annealing temperature plot [Fig. 2(c)]. Thus, the hardening behavior that we report is conservative, and yet, we measure sizable evolution in the hardness within a given alloy and among alloys of different composition. Taken as a whole, the evolution of the lattice parameter is a strong indicator of synergistic co-segregation of Ni and Ce to the GBs and subsequent relaxation processes. These results are not only consistent with solute partitioning observed in previous investigations of Al–Ni–Ce nanocrystalline alloys [20, 21], but also other Al-based nanocrystalline/amorphous alloys [87, 88]. As the GB properties often determine the mechanical response of NC alloys, the distinctively different strengthening behavior between 3.1 and 7.2 at.% alloy can be attributed to the amount of Ni + Ce enriched at the GBs. The stability of the nanostructure in these alloys to technologically relevant service temperatures is notable, and the compositional dependence of both the anneal-hardened state and the temperatures to which mechanical strength is maintained suggests a very flexible design space in this alloy system.

Further annealing at higher temperatures > 300 °C led to a pronounced evolution of the nanocrystalline microstructures, including the development of secondary phases and concurrent grain growth. The most noticeable hardness drops for each composition [Fig. 4(a)] corresponded with the onset of grain growth [Fig. 4(b)]. Annealing at 350 °C for 2 h induced pronounced grain growth with mean sizes evolving from 18 to 35 nm in the 3.1 at.% alloy, which coincided with the loss of 55% of the hardness (from 4.24 to 2.32 GPa). Further annealing to 375 °C triggered additional grain growth to 55 nm, further decreasing the strength to 2.21 GPa. In contrast, the 7.2 at.% alloy did not undergo significant grain growth or a hardness drop after annealing at 350 °C, and the first measurable indication of grain growth in the 7.2 at.% alloy was observed after annealing at 375 °C ($0.7T_m$). This result suggests an exceptionally stable NC Al alloy, since most NC Al alloys have been reported to soften at temperatures well below 350 °C [78]. At these elevated temperatures, the mean grain size grew from 10 to 40 nm, and the hardness dropped; nevertheless, the hardening brought out by annealing at lower temperatures was somewhat retained, leading

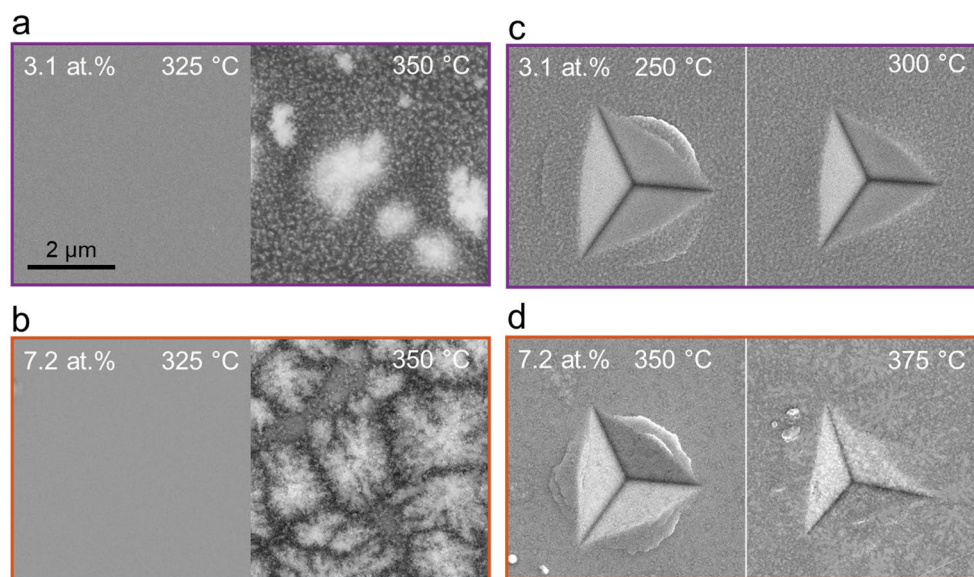


Figure 5: BSE images of before and after the precipitation of secondary phases in (a) 3.1 at% and (b) 7.2 at% alloy. SE images near the indents before and after the suppression of shear localization in (c) 3.1 at% and (d) 7.2 at% alloy. The micrographs share the same scale bar.

to a 7.5% higher hardness over the as-deposited state despite the grain growth. Consistent with the lattice parameter data, the enrichment of Ni+Ce at the GBs further stabilizes the NC structure and the final strength following a thermal exposure at 70% of the melting temperature of Al.

Intermetallic precipitation and shear localization

Precipitation of second phases occurred in both 3.1 at.% and 7.2 at.% alloys after annealing at 350 °C ($0.67T_m$), as evidenced by backscattered electron (BSE) images [Fig. 5(a) and (b)]. The occurrence of a second phase is known to disrupt the GB enriched state by consuming the segregated solutes during the formation of intermetallic compounds, which can destabilize the microstructure and lead to grain growth. Such a phase separation event triggering grain growth was observed in the 3.1 at.% alloy [Fig. 4(b)], which coincides with a significant drop in hardness. Previous work investigating an Al–Ni–Ce alloy demonstrated that the nucleation of $Al_{11}Ce_3$ and Al_3Ni phases, as determined by combined electron diffraction and EDS elemental mapping, sufficiently consumed grain boundary solute to allow significant grain growth and cause a concomitant decrease in hardness [20, 21]. Both Ni and Ce have negligible solubility in Al and are reported to readily form $Al_{11}Ce_3$ and Al_3Ni intermetallic phases [21, 89, 90]. At the same time, Al–Ni–Ce is an effective glass-forming system [58]. Therefore, Ni and Ce segregated to the GB can form energetically favorable AIFs when annealed and subsequently quenched [20], which then competes with intermetallic formation at an

elevated temperature. Recent X-ray total scattering experiments demonstrated that the Ni and Ce enrichment in the AIFs causes destabilization of Ni- and Ce-centered, polyhedral, medium-range order in the amorphous regions of the material, hindering intermetallic precipitation [21]. The observation from the 350 °C annealing experiment suggests that higher alloying content at the GB hampers the nucleation and growth of the second phase. In turn, it prevents runaway precipitation, and the grain size is retained in the remaining matrix to sustain the strength after being exposed at higher temperatures.

We next turn our attention to the influence of the GB chemistry and structural state on the progression of plasticity and potential for damage tolerance in this class of alloys. Keeping in mind that the abundance of GBs contributes to the mechanical response in NC alloys, we estimate the GB fractions of the 3.1 at.% and 7.2 at.% alloys to be 11.3% and 26.1%, respectively, assuming 2D hexagonal grains and a GB thickness of 1 nm [21]. This non-negligible fraction of atoms residing in GB regions not only acts as an obstacle to dislocation glides but also can serve as dislocation nucleation sites and plasticity carriers by activating GB rotation and sliding [3, 69–71, 73]. The operation of GB-mediated deformation mechanisms often induces unfavorable shear localization [91, 92], which precludes homogeneous plastic flow and ultimately damage tolerance. In the current study, all the as-deposited Al–Ni–Ce alloys experienced localized plasticity which manifests as shear bands in the vicinity of the indent marks. However, after annealing at 300 °C for 2 h, evidence of shear localization diminished in the 3.1 at.% alloy [Fig. 5(c)] with only a marginal decrease of hardness from

the 250 °C annealed state [Fig. 4(a)], where shear localization was rampant [Fig. 5(c)]. While thermal relaxation can increase the strength at the expense of strain to failure at in some NC alloys [92, 93], this tradeoff was recently circumvented in the Al–Ni–Ce system [20]. These researchers ascribed the suppression of shear localization to a segregation-induced stiff intergranular film and compliant grain interior that facilitates dislocation activities over GB sliding, with the latter promoting shear banding. In the present study, the 7.2 at.% alloy hosts shear localization behavior persisting up to an annealing temperature of 350 °C, at which point grain growth was suppressed while intermetallic compounds precipitated. The persistence of shear localization can be hypothesized to be a result of an insufficient portion of compliant grain interior, due to the very small grain size (< 10 nm), required to transition deformation mechanisms. However, evidence of shear localization in the 7.2 at.% alloy disappeared after 375 °C annealing, where the fraction of intermetallic compounds further increases to induce grain growth. While this more homogeneous plastic response comes at the expense of a drop in hardness relative to the peak anneal-hardened value, the resulting hardness in the evolved state is still higher than the as-deposited value, highlighting the importance of the interfacial segregation and presumed formation of unique GB states in governing the pathways for subsequent microstructural evolution. These results demonstrate how one could optimize the thermomechanical response of these lightweight alloys through subtle compositional tuning and judicious selection of heat treatments.

Influence of extended annealing

Kinetics play an influential role in GB segregation and intermetallic formation that determines the final structure and mechanical properties; accordingly, we examined the effect of annealing time on the interrelationship between microstructure and mechanical behavior. In the representative 3.1 at.% alloy, an increase of annealing time decreased the transition temperature to shear localization. The shear bands near the indents disappeared at 200 °C when annealed for 16 h [Fig. 6(a)], and are associated with a small decrease of hardness. In contrast, increasing the annealing time in the 7.2 at.% alloy from 2 to 16 h led to a hardness increase from 4.19 to 4.48 GPa [Fig. 5(f)] with no change in shear localization behavior [Fig. 6(b)]. A 16 h annealing of 7.2 at.% at 287 °C ($0.6T_m$) precipitated intermetallic compounds [Fig. 6(c)], suggesting kinetic effects on phase separation at elevated temperature, consistent with a large activation energy for precipitation from a confined AIF in an Al–Ni–Ce NC alloy [21]. While the hardness does decrease relative to the 2 h annealing treatment at 250 °C and 300 °C, it remains significantly higher than the initial hardness, and the prolonged annealing suppressed the shear localization. Annealing at 325 °C followed by an air quench introduced shear localization in the 3.1 at.% [Fig. 6(d)] and lowered the strength [Fig. 6(f)], implying that the segregation-mediated mechanism of GB stiffening requires longer time or higher temperature. For the 7.2 at.% alloy, there was a negligible effect of rapid cooling from 325 °C on shear localization [Fig. 6(e)]. The 16 h annealing results suggest that extended annealing at a lower temperature can often be beneficial, especially in suppressing shear localization without significantly compromising

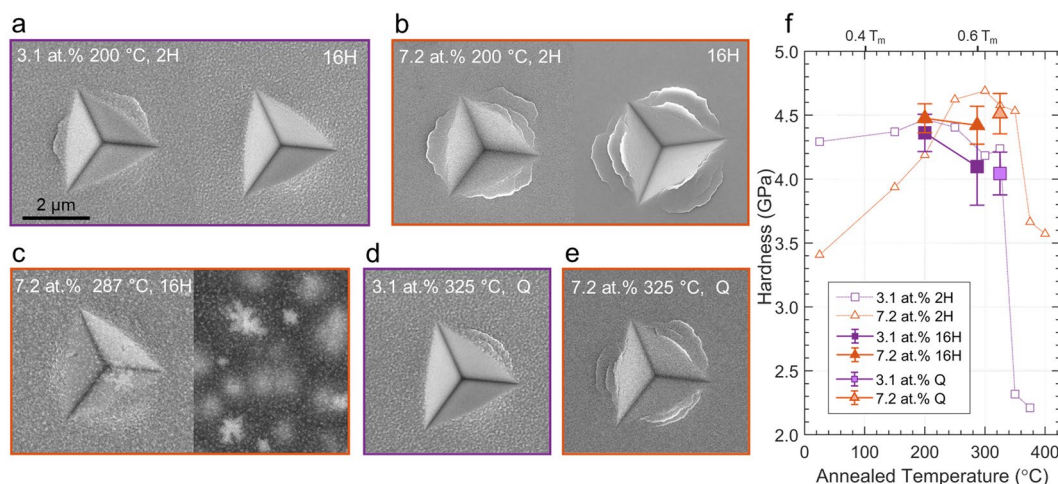


Figure 6: SE image of indentation morphology taken after 2-h and 16-h annealing at 200 °C of (a) 3.1 at% and (b) 7.2 at% alloy. (c) 7.2 at% alloy annealed at 287 °C ($0.6T_m$) for 16 h. Indentation morphology of air-quenched 325 °C annealed (d) 3.1 at% and (e) 7.2 at% alloy. The micrographs share the same scale bar. (f) Hardness plot of 3.1 at% and 7.2 at% alloys with varying annealing conditions.

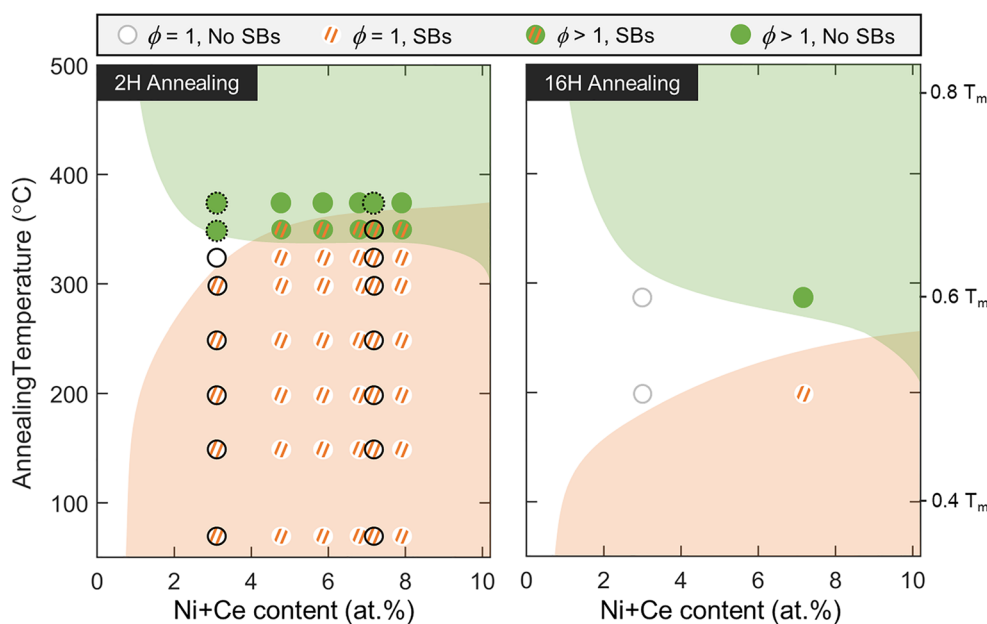


Figure 7: A schematic diagram of segregation-induced engineering space for nanocrystalline Al–Ni–Ce alloys with 2 h (2H) and 16 h (16H) annealing time. The area is divided based on the number of phase (ϕ) and the presence of shear bands (SB). The experimental data are overlaid with symbols. The solid and dotted black outlines of the symbols indicate grain size retention and grain growth confirmed by XRD, respectively.

the strength, which collectively enhances thermal stability and mechanical behavior in concert.

Discussion

Finally, we aggregate our collective results to demonstrate the strong dependence of alloying content in the Al–Ni–Ce NC system on thermal stability and phase evolution, hardness retention following thermal exposure, and plastic localization behavior to generate mechanism maps to demarcate the NC alloy design space. Three experimentally validated boundaries delineate sub-regions in the maps constructed for 2 h of annealing (left panel of Fig. 7) associated with: intermetallic compound precipitation with the number of phases (ϕ) greater than 1 (solid green), shear localization (solid orange), and grain growth (dotted gray).

The area above the intermetallic formation line depicts the temperature and composition threshold for precipitation of second phases $\phi > 1$. While the transition temperature for phase transformation in the absence of GB segregation would be expected to decrease since the driving force to form intermetallic compounds increases with alloying content in the bulk phase diagram, the slope of the boundary is relatively flat in the NC alloys between 3 to 8 at.% of alloying content, as all the alloys that we explored precipitated second phases after annealing at 350 °C for 2 h. Thus, the co-segregation of both Ni and Ce to the GB hinders phase separation, providing thermal stability to relatively high temperatures. The

shear localization boundary divides the compositional and temperature regions where shear bands are suppressed after the indentations. Annealing to sufficiently high temperatures promote more homogeneous plasticity, even in cases where the microstructure is stable, suggesting that some amount of segregation facilitates both hardness increases and stable plastic flow. The transition temperature of this boundary increases as the Ni + Ce level increases, as evidenced by the micrographs of surface morphology [Fig. 5(c) and (d)]. At leaner compositions, the transition temperature decreases sharply as the nanostructure is unstable, and pronounced grain growth generally eliminates shear localization at the expense of strength. With a minimal increase in annealing temperature from 350 to 375 °C, the transition temperature is relatively insensitive to the alloying content, which can be attributed to the efficacy of segregation engineering in this alloy. Notably, the plateau in the intermetallic precipitation line highlights that fine tuning of alloying elements added to the NC material can boost thermal stability substantially.

The crossover between the intermetallic precipitation and shear localization boundaries delineates four unique areas: single phase ($\phi = 1$) with and without shear bands and multiphase ($\phi > 1$) with and without shear bands. The crossover point is at approximately Ni + Ce = 5.5 at.% and at 350 °C in the 2-h annealing diagram. This defines an optimal alloy composition and heat treatment at leaner compositions from the crossover point that maintains stable NC grains without shear localization. One can further note a small window (bounded by the strength

retention line) where the alloy maintains a strength above its initial strength together with the aforementioned features. Below the crossover point, the alloy undergoes substantial hardening owing to GB segregation, as demonstrated in Fig. 2(c) at the expense of the shear band formation. Above the crossover point, alloys precipitate second phases yet are expected to undergo uniform plastic deformation. Grain growth can be hindered even following second-phase precipitation at an adequately higher Ni + Ce level as confirmed in the previous grain size analysis [Fig. 4(b)], likely due to residual solute at grain boundaries or a high concentration of intermetallic particles. Thus, both high strength and the potential for damage tolerance is possible with the aid of nano-scaled intermetallic precipitates. Finally, an alloy with high Ni and Ce content heat treated to reside at higher compositions from the crossover point precipitates second phases and experiences unfavorable shear localization.

The experimental observations in Fig. 6 suggest varying annealing times transform the characteristic regions. The intermetallic precipitation line and the shear localization line shift to lower temperatures at increased annealing time to 16 h. Consequently, the single-phase area without shear localization can expand (right panel in Fig. 7). Both the temperature range and Ni + Ce level limit increase, bolstering the opportunity to utilize segregation engineering in potentially ductile NC alloys.

Conclusions

A combinatorial approach and high throughput characterization methods were employed to explore the composition space of a segregation-engineered Al-rich ternary nanocrystalline system. Two separate sputtering configurations were utilized, from which 30 initial alloys with varying Ni + Ce content were down-selected to 6 alloys covering a range of composition (3.1 at.% to 7.8 at.%) to monitor the characteristic mechanical behavior following thermal excursions. As a result, two representative behaviors were identified to focus on investigating solute segregation effects on the thermal stability and mechanical behavior of Al–Ni–Ce nanocrystalline alloys. The key findings of the current study are as follows:

- The mechanical strength responding to the annealing temperatures is a strong function of alloying content. Tailoring the Ni + Ce content from lean to enriched promotes hardening behavior and increases the strength after microstructural evolution.
- Despite the precipitation of second phases after annealing at $0.67T_m$, alloying contents of 6.8 at.% and above retain their strength above that of their corresponding initial strength.
- A sufficient amount of co-segregating species gives rise to the coexistence of grain size retention with precipitation of second phases.

- While a higher alloying content gives rise to higher strength with the formation of shear bands, a longer annealing time mitigates localized plasticity without compromising strength.
- The interplay between segregation, microstructural evolution, and the resulting thermal stability and mechanical behavior can be illustrated by mapping four characteristic regimes in composition-temperature space.

The exceptional thermal stability of the Al–Ni–Ce system via segregation engineering evokes several promising avenues for other Al-rich nanocrystalline alloys for high-temperature applications. The mapping of characteristic properties brought about by segregation phenomena in compositional and processing space also promises to accelerate the wider use of nanocrystalline alloys. For instance, outcomes from a combinatorial synthesis and rapid characterization effort could efficiently down-select promising compositions and inform design parameters to synthesize bulk NC alloys at industrial scales, for example, through mechanical alloying.

Materials and methods

Al–Ni–Ce NC alloys were synthesized using an AJA ATC 1800 sputter deposition system configured with a pure Al target (99.999%) and a pre-alloyed Al-7 at.% Ni-6 at.% Ce target (99.95%) at a base pressure of 1.33×10^{-8} mbar. The working pressure and substrate temperature were maintained at 4 mbar ($3.0 \times \text{mTorr}$) and 25–30 °C, respectively. The deposition was interrupted every 40 s for a duration of 8 s to reduce the aspect ratio of NC grains following the method in [20]. Alloys were sputtered to 1 μm thicknesses on (100) Si wafers for mechanical testing and onto glass substrates for XRD scans. The deposition thickness assures the sample to contain ~ 100 grains in the indentation direction, thus, representing bulk behavior. Indentation tests were performed using a KLA iMicro Nanoindenter equipped with a 50 mN load cell and a diamond Berkovich tip. A dynamic oscillation with an amplitude of 1 nm was superimposed at 100 Hz for continuous stiffness measurements during indentation at a strain rate of 0.2 s^{-1} . The reported hardness values were averaged from 100 to 150 nm indentation depths to avoid the effects of surface roughness and the influence of the substrate. XRD scans were performed on a Rigaku SmartLab diffractometer using a $\text{Cu K}\alpha_1$ source. Lattice parameter (a) and mean grain size (d) of the Al-rich alloys were determined from fitting the profile of the {111} peak [94] and the coherently scattered length from Scherrer equation [95]. The residual stress was assessed using the $\sin^2\psi$ method, as described in detail in Refs. [83, 96]. Our previous

investigations into one specific Al–Ni–Ce alloy [21], as well as 3 other related Al ternary nanocrystalline alloys [97], corroborated the accuracy of the XRD-determined mean grain sizes using direct TEM grain size measurements, demonstrating that heterogeneous strain from dislocations and residual stresses are negligible in their contributions to peak broadening [20]. The nominal composition of the deposited films was measured by SEM–EDS. 2D mapping (250 μm by 250 μm) was performed at multiple positions ($n > 5$) of a patch. We chose the combination of characterization and analysis techniques used in the present work to optimize experimental throughput with the goal of rapidly searching through composition and annealing space.

Funding

This material is based upon work supported by the U.S. Department of Energy’s Office of Energy Efficiency and Renewable Energy (EERE) under the Advanced Manufacturing Office Award Number DE-EE0009114. GHB acknowledges support from the National Science Foundation Graduate Research Fellowship under Grant No. 1650114. This work employed the MRL Shared Experimental Facilities at UC Santa Barbara, which are supported by the MRSEC Program of the NSF under Award No. DMR 1720256; a member of the NSF-funded Materials Research Facilities Network (www.mrnf.org).

Data availability

Data will be made available on reasonable request.

Code availability

Not applicable.

Declarations

Conflict of interest Not applicable.

References

1. D. Raabe, M. Herbig, S. Sandlöbes, Y. Li, D. Tytko, M. Kuzmina, D. Ponge, P.-P. Choi, Grain boundary segregation engineering in metallic alloys: A pathway to the design of interfaces. *Curr. Opin. Solid State Mater. Sci.* **18**, 253–261 (2014). <https://doi.org/10.1016/j.COSSMS.2014.06.002>
2. T.J. Rupert, The role of complexions in metallic nano-grain stability and deformation. *Curr. Opin. Solid State Mater. Sci.* **20**, 257–267 (2016). <https://doi.org/10.1016/j.COSSMS.2016.05.005>
3. T.J. Rupert, D.S. Gianola, Y. Gan, K.J. Hemker, Experimental observations of stress-driven grain boundary migration. *Science* **326**, 1686–1690 (2009)
4. M.-R. He, S.K. Samudrala, G. Kim, P.J. Felfel, A.J. Breen, J.M.C. Cairney, D.S. Gianola, J.M.C. Cairney, Linking stress-driven microstructural evolution in nanocrystalline aluminium with grain boundary doping of oxygen. *Nat Commun* **7**, 1–7 (2016). <https://doi.org/10.1038/pj.2016.37>
5. R.I. Babicheva, S.V. Dmitriev, L. Bai, Y. Zhang, S.W. Kok, G. Kang, K. Zhou, Effect of grain boundary segregation on the deformation mechanisms and mechanical properties of nanocrystalline binary aluminum alloys. *Comput. Mater. Sci.* **117**, 445–454 (2016). <https://doi.org/10.1016/j.commatsci.2016.02.013>
6. H.A. Murdoch, C.A. Schuh, Estimation of grain boundary segregation enthalpy and its role in stable nanocrystalline alloy design. *J. Mater. Res.* **28**, 2154–2163 (2019). <https://doi.org/10.1557/jmr.2013.211>
7. J.F. Nie, Y.M. Zhu, J.Z. Liu, X.Y. Fang, Periodic segregation of solute atoms in fully coherent twin boundaries. *Science* **340**, 957–960 (2013). <https://doi.org/10.1126/science.1229369>
8. A. Devaraj, W. Wang, R. Vemuri, L. Kovarik, X. Jiang, M. Bowden, J.R.R. Trelewicz, S. Mathaudhu, A. Rohatgi, Grain boundary segregation and intermetallic precipitation in coarsening resistant nanocrystalline aluminum alloys. *Acta Mater.* **165**, 698–708 (2019). <https://doi.org/10.1016/j.actamat.2018.09.038>
9. K.A. Darling, M. Rajagopalan, M. Komarasamy, M.A. Bhatia, B.C. Hornbuckle, R.S. Mishra, K.N. Solanki, Extreme creep resistance in a microstructurally stable nanocrystalline alloy. *Nature* **537**, 378–381 (2016). <https://doi.org/10.1038/nature19313>
10. T. Frolov, K.A. Darling, L.J. Kecskes, Y. Mishin, Stabilization and strengthening of nanocrystalline copper by alloying with tantalum. *Acta Mater.* **60**, 2158–2168 (2012). <https://doi.org/10.1016/j.ACTAMAT.2012.01.011>
11. C.C. Koch, R.O. Scattergood, K.A. Darling, J.E. Semones, Stabilization of nanocrystalline grain sizes by solute additions. *J. Mater. Sci.* **43**, 7264–7272 (2008). <https://doi.org/10.1007/s10853-008-2870-0>
12. K.A. Darling, B.K. VanLeeuwen, C.C. Koch, R.O. Scattergood, Thermal stability of nanocrystalline Fe–Zr alloys. *Mater. Sci. Eng. A* **527**, 3572–3580 (2010). <https://doi.org/10.1016/j.msea.2010.02.043>
13. Y. Hu, T.J. Rupert, Atomistic modeling of interfacial segregation and structural transitions in ternary alloys. *J. Mater. Sci.* **54**, 3975–3993 (2019). <https://doi.org/10.1007/s10853-018-3139-x>
14. W. Xing, A.R. Kalidindi, D. Amram, C.A. Schuh, Solute interaction effects on grain boundary segregation in ternary alloys. *Acta Mater.* **161**, 285–294 (2018). <https://doi.org/10.1016/j.actamat.2018.09.005>
15. A.L. Vasiliev, M. Aindow, M.J. Blackburn, T.J. Watson, Phase stability and microstructure in devitrified Al-rich Al–Y–Ni alloys. *Intermetallics* **12**, 349–362 (2004). <https://doi.org/10.1016/j.intermet.2003.11.007>

16. Y.H. Gao, L.F. Cao, J. Kuang, H. Song, G. Liu, J.Y. Zhang, J. Sun, Solute repositioning to tune the multiple microalloying effects in an Al–Cu alloy with minor Sc, Fe and Si addition. *Mater. Sci. Eng. A* **803**, 140509 (2021). <https://doi.org/10.1016/j.msea.2020.140509>
17. C.M. Grigorian, T.J. Rupert, Thick amorphous complexion formation and extreme thermal stability in ternary nanocrystalline Cu–Zr–Hf alloys. *Acta Mater.* **179**, 172–182 (2019)
18. J.D. Schuler, T.J. Rupert, Materials selection rules for amorphous complexion formation in binary metallic alloys. *Acta Mater.* **140**, 196–205 (2017)
19. A. Khalajhedayati, T.J. Rupert, High-temperature stability and grain boundary complexion formation in a nanocrystalline Cu–Zr alloy. *JOM* **67**, 2788–2801 (2015). <https://doi.org/10.1007/s11837-015-1644-9>
20. G.H. Balbus, F. Wang, D.S. Gianola, Suppression of shear localization in nanocrystalline Al–Ni–Ce via segregation engineering. *Acta Mater.* **188**, 63–78 (2020). <https://doi.org/10.1016/j.actamat.2020.01.041>
21. G.H. Balbus, J. Kappacher, D.J. Sprouster, F. Wang, J. Shin, Y.M. Eggeler, T.J. Rupert, J.R. Trelewicz, D. Kiener, V. Maier-Kiener, D.S. Gianola, Disordered interfaces enable high temperature thermal stability and strength in a nanocrystalline aluminum alloy. *Acta Mater.* (2021). <https://doi.org/10.1016/j.actamat.2021.116973>
22. F. Liu, R. Kirchheim, Nano-scale grain growth inhibited by reducing grain boundary energy through solute segregation. *J. Cryst. Growth* **264**, 385–391 (2004). <https://doi.org/10.1016/j.jcrysgro.2003.12.021>
23. R. Kirchheim, Grain coarsening inhibited by solute segregation. *Acta Mater.* **50**, 413–419 (2002). [https://doi.org/10.1016/S1359-6454\(01\)00338-X](https://doi.org/10.1016/S1359-6454(01)00338-X)
24. J. Weissmüller, Alloy effects in nanostructures. *Nanostruct. Mater.* **3**, 261–272 (1993). [https://doi.org/10.1016/0965-9773\(93\)90088-S](https://doi.org/10.1016/0965-9773(93)90088-S)
25. T. Chookajorn, H.A. Murdoch, C.A. Schuh, Design of stable nanocrystalline alloys. *Science* **337**, 951–954 (2012). <https://doi.org/10.1126/science.1224737>
26. J.R. Trelewicz, C.A. Schuh, Grain boundary segregation and thermodynamically stable binary nanocrystalline alloys. *Phys. Rev.* **79**, 094112 (2009). <https://doi.org/10.1103/PhysRevB.79.094112>
27. C.E. Krill III, R. Klein, S. Janes, R. Birringer, Thermodynamic stabilization of grain boundaries in nanocrystalline alloys. *Mater. Sci. Forum* **179–181**, 443–448 (1995). <https://doi.org/10.4028/www.scientific.net/MSF.179-181.443>
28. M. Saber, H. Kotan, C.C. Koch, R.O. Scattergood, Thermodynamic stabilization of nanocrystalline binary alloys. *J. Appl. Phys.* **113**, 063515 (2013). <https://doi.org/10.1063/1.4791704>
29. K.A. Darling, M.A. Tschopp, R.K. Guduru, W.H. Yin, Q. Wei, L.J. Kecskes, Microstructure and mechanical properties of bulk nanostructured Cu–Ta alloys consolidated by equal channel angular extrusion. *Acta Mater.* **76**, 168–185 (2014). <https://doi.org/10.1016/j.actamat.2014.04.074>
30. A. Michels, C.E. Krill, H. Ehrhardt, R. Birringer, D.T. Wu, Modelling the influence of grain-size-dependent solute drag on the kinetics of grain growth in nanocrystalline materials. *Acta Mater.* **47**, 2143–2152 (1999). [https://doi.org/10.1016/S1359-6454\(99\)00079-8](https://doi.org/10.1016/S1359-6454(99)00079-8)
31. M. Rajagopalan, K. Darling, S. Turnage, R.K. Koju, B. Hornbuckle, Y. Mishin, K.N. Solanki, Microstructural evolution in a nanocrystalline Cu–Ta alloy: A combined in-situ TEM and atomistic study. *Mater. Des.* **113**, 178–185 (2017). <https://doi.org/10.1016/j.matdes.2016.10.020>
32. M.A. Atwater, R.O. Scattergood, C.C. Koch, The stabilization of nanocrystalline copper by zirconium. *Mater. Sci. Eng.: A* **559**, 250–256 (2013). <https://doi.org/10.1016/j.msea.2012.08.092>
33. R.K. Koju, K.A. Darling, K.N. Solanki, Y. Mishin, Atomistic modeling of capillary-driven grain boundary motion in Cu–Ta alloys. *Acta Mater.* (2018). <https://doi.org/10.1016/j.actamat.2018.01.027>
34. P.R. Cantwell, M. Tang, S.J. Dillon, J. Luo, G.S. Rohrer, M.P. Harmer, Grain boundary complexions. *Acta Mater.* **62**, 1–48 (2014). <https://doi.org/10.1016/j.actamat.2013.07.037>
35. S.J. Dillon, M. Tang, W.C. Carter, M.P. Harmer, Complexion: A new concept for kinetic engineering in materials science. *Acta Mater.* **55**, 6208–6218 (2007). <https://doi.org/10.1016/J.ACTAMAT.2007.07.029>
36. J.D. Schuler, O.K. Donaldson, T.J. Rupert, Amorphous complexions enable a new region of high temperature stability in nanocrystalline Ni–W. *Scr. Mater.* **154**, 49–53 (2018). <https://doi.org/10.1016/J.SCRIPTAMAT.2018.05.023>
37. G. Sha, L. Yao, X. Liao, S.P. Ringer, Z.C. Duan, T.G. Langdon, Segregation of solute elements at grain boundaries in an ultrafine grained Al–Zn–Mg–Cu alloy. *Ultramicroscopy* **111**, 500–505 (2011). <https://doi.org/10.1016/J.ULTRAMIC.2010.11.013>
38. M. Hans, P. Keuter, A. Saksena, J.A. Sälker, M. Momma, H. Springer, J. Nowak, D. Zander, D. Primetzhofer, J.M. Schneider, Opportunities of combinatorial thin film materials design for the sustainable development of magnesium-based alloys. *Sci. Rep.* (2021). <https://doi.org/10.1038/s41598-021-97036-6>
39. R. Pei, Y. Zou, D. Wei, T. Al-Samman, Grain boundary co-segregation in magnesium alloys with multiple substitutional elements. *Acta Mater.* **208**, 116749 (2021). <https://doi.org/10.1016/j.actamat.2021.116749>
40. C.Y. Wang, L.W. Yang, Y.W. Cui, M.T. Pérez-Prado, High throughput analysis of solute effects on the mechanical behavior and slip activity of beta titanium alloys. *Mater. Des.* **137**, 371–383 (2018). <https://doi.org/10.1016/J.MATDES.2017.10.029>
41. R. Schoeppner, C. Ferguson, L. Pethö, C. Guerra-Nuñez, A.A. Taylor, M. Polyakov, B. Putz, J.M. Breguet, I. Utke, J. Michler, Interfacial adhesion of alumina thin films over the full

- compositional range of ternary fcc alloy films: A combinatorial nanoindentation study. *Mater. Des.* **193**, 108802 (2020). <https://doi.org/10.1016/j.matdes.2020.108802>
42. S.-I. Jun, P.D. Rack, T.E. McKnight, A.V. Melechko, M.L. Simpson, Electrical and microstructural characterization of molybdenum tungsten electrodes using a combinatorial thin film sputtering technique. *J. Appl. Phys.* **97**, 054906 (2005). <https://doi.org/10.1063/1.1855395>
 43. T. Iwasaki, N. Itagaki, T. Den, H. Kumomi, K. Nomura, T. Kamiya, H. Hosono, Combinatorial approach to thin-film transistors using multicomponent semiconductor channels: An application to amorphous oxide semiconductors in In–Ga–Zn–O system. *Appl. Phys. Lett.* **90**, 242114 (2007). <https://doi.org/10.1063/1.2749177>
 44. P. Ziolkowski, M. Wambach, A. Ludwig, E. Mueller, Application of high-throughput seebeck microprobe measurements on thermoelectric half-Heusler thin film combinatorial material libraries. *ACS Comb. Sci.* **20**, 1–18 (2018). <https://doi.org/10.1021/acscombsci.7b00019>
 45. R. Collette, Y. Wu, A. Olafsson, J.P. Camden, P.D. Rack, Combinatorial thin film sputtering AuxAl_{1-x} alloys: Correlating composition and structure with optical properties. *ACS Comb. Sci.* **20**, 633–642 (2018). <https://doi.org/10.1021/ACSCOMBSCI.8B00091>
 46. A. Ludwig, N. Zotov, A. Savan, S. Groudeva-Zotova, Investigation of hard magnetic properties in the Fe–Pt system by combinatorial deposition of thin film multilayer libraries. *Appl. Surf. Sci.* **252**, 2518–2523 (2006). <https://doi.org/10.1016/j.apsusc.2005.04.058>
 47. A. Marshal, K.G. Pradeep, D. Music, L. Wang, O. Petravic, J.M. Schneider, Combinatorial evaluation of phase formation and magnetic properties of FeMnCoCrAl high entropy alloy thin film library. *Sci. Rep.* (2019). <https://doi.org/10.1038/s41598-019-44351-8>
 48. J. Li, F.S. Gittleson, Y. Liu, J. Liu, A.M. Loye, L. McMillon-Brown, T.R. Kyriakides, J. Schroers, A.D. Taylor, Exploring a wider range of Mg–Ca–Zn metallic glass as biocompatible alloys using combinatorial sputtering. *Chem. Commun.* **53**, 8288–8291 (2017). <https://doi.org/10.1039/C7CC02733H>
 49. J.M. Gregoire, P.J. McCluskey, D. Dale, S. Ding, J. Schroers, J.J. Vlassak, Combining combinatorial nanocalorimetry and X-ray diffraction techniques to study the effects of composition and quench rate on Au–Cu–Si metallic glasses. *Scr. Mater.* **66**, 178–181 (2012). <https://doi.org/10.1016/J.SCRIPTAMAT.2011.10.034>
 50. J.H. Yao, C. Hostert, D. Music, A. Frisk, M. Björck, J.M. Schneider, Synthesis and mechanical properties of Fe–Nb–B thin-film metallic glasses. *Scr. Mater.* **67**, 181–184 (2012). <https://doi.org/10.1016/J.SCRIPTAMAT.2012.04.011>
 51. S. Ding, J. Gregoire, J.J. Vlassak, J. Schroers, Solidification of Au–Cu–Si alloys investigated by a combinatorial approach. *J. Appl. Phys.* **111**, 114901 (2012). <https://doi.org/10.1063/1.4722996>
 52. A. Marshal, K.G. Pradeep, D. Music, S. Zaefferer, P.S. De, J.M. Schneider, Combinatorial synthesis of high entropy alloys: Introduction of a novel, single phase, body-centered-cubic FeMnCoCrAl solid solution. *J. Alloys Compd.* **691**, 683–689 (2017). <https://doi.org/10.1016/J.JALLCOM.2016.08.326>
 53. Z. Li, A. Ludwig, A. Savan, H. Springer, D. Raabe, Combinatorial metallurgical synthesis and processing of high-entropy alloys. *J. Mater. Res.* **33**, 3156–3169 (2018). <https://doi.org/10.1557/jmr.2018.214>
 54. S.A. Kube, S. Sohn, D. Uhl, A. Datye, A. Mehta, J. Schroers, Phase selection motifs in high entropy alloys revealed through combinatorial methods: Large atomic size difference favors BCC over FCC. *Acta Mater.* **166**, 677–686 (2019). <https://doi.org/10.1016/J.ACTAMAT.2019.01.023>
 55. D.B. Miracle, M. Li, Z. Zhang, R. Mishra, K.M. Flores, Emerging capabilities for the high-throughput characterization of structural materials. *Annu. Rev. Mater. Res.* **51**, 131–164 (2021). <https://doi.org/10.1146/ANNUREV-MATSCI-080619-022100>
 56. S.A. Kube, W. Xing, A. Kalidindi, S. Sohn, A. Datye, D. Amram, C.A. Schuh, J. Schroers, Combinatorial study of thermal stability in ternary nanocrystalline alloys. *Acta Mater.* **188**, 40–48 (2020). <https://doi.org/10.1016/j.actamat.2020.01.059>
 57. Y.J. Li, A. Kostka, A. Savan, A. Ludwig, Phase decomposition in a nanocrystalline CrCoNi alloy. *Scr. Mater.* **188**, 259–263 (2020). <https://doi.org/10.1016/J.SCRIPTAMAT.2020.07.054>
 58. A. Inoue, H. Kimura, Fabrications and mechanical properties of bulk amorphous, nanocrystalline, nanoquasicrystalline alloys in aluminum-based system. *J. Light Met.* **1**, 31–41 (2001). [https://doi.org/10.1016/S1471-5317\(00\)00004-3](https://doi.org/10.1016/S1471-5317(00)00004-3)
 59. C.V. Thompson, R. Carel, Texture development in polycrystalline thin films. *Mater. Sci. Eng., B* **32**, 211–219 (1995). [https://doi.org/10.1016/0921-5107\(95\)03011-5](https://doi.org/10.1016/0921-5107(95)03011-5)
 60. R.K. Gupta, B.S. Murty, N. Birbilis, *An Overview of High-Energy Ball Milled Nanocrystalline Aluminum Alloys* (Springer, Cham, 2017)
 61. L. Ajdelsztajn, B. Jodoin, G.E. Kim, J.M. Schoenung, Cold spray deposition of nanocrystalline aluminum alloys. *Metall. Mater. Trans. A* **36**, 657–666 (2005)
 62. F. Endres, M. Bukowski, R. Hempelmann, H. Natter, Electrodeposition of nanocrystalline metals and alloys from ionic liquids. *Angew. Chem. Int. Ed.* **42**, 3428–3430 (2003). <https://doi.org/10.1002/anie.200350912>
 63. C.V. Thompson, Grain growth in thin films. *Annu. Rev. Mater. Sci.* **20**, 245–268 (1990). <https://doi.org/10.1063/1.3058054>
 64. M. Ohring, *Materials Science of Thin Films* (Elsevier, Amsterdam, 2001)
 65. H. Okamoto, Al–Ni (Aluminum–Nickel). *J. Phase Equilib.* **14**, 257 (1993)

66. K.A. Gschneidner, F.W. Calderwood, The Al-Ce (Aluminum-Cerium) System Equilibrium Diagram, n.d.
67. K. Maung, J.C. Earthman, F.A. Mohamed, Inverse Hall-Petch behavior in diamantane stabilized bulk nanocrystalline aluminum. *Acta Mater.* **60**, 5850–5857 (2012). <https://doi.org/10.1016/j.actamat.2012.07.026>
68. Y. Ito, K. Edalati, Z. Horita, High-pressure torsion of aluminum with ultrahigh purity (99.9999%) and occurrence of inverse Hall-Petch relationship. *Mater. Sci. Eng. A* **679**, 428–434 (2017). <https://doi.org/10.1016/j.msea.2016.10.066>
69. J. Schiøtz, K.W. Jacobsen, A maximum in the strength of nanocrystalline copper. *Science* **301**, 1357–1359 (2003). <https://doi.org/10.1126/SCIENCE.1086636>
70. L. Wang, J. Teng, P. Liu, A. Hirata, E. Ma, Z. Zhang, M. Chen, X. Han, Grain rotation mediated by grain boundary dislocations in nanocrystalline platinum. *Nat. Commun.* (2014). <https://doi.org/10.1038/ncomms5402>
71. Z. Shan, E.A. Stach, J.M.K. Wiezorek, J.A. Knapp, D.M. Follstaedt, S.X. Mao, Grain boundary-mediated plasticity in nanocrystalline nickel. *Science* **305**, 654–657 (2004). <https://doi.org/10.1126/science.1098741>
72. T.J. Rupert, J.R. Trelewicz, C.A. Schuh, Grain boundary relaxation strengthening of nanocrystalline Ni–W alloys. *J. Mater. Res.* **27**, 1285–1294 (2012). <https://doi.org/10.1557/jmr.2012.55>
73. J. Hu, Y.N. Shi, X. Sauvage, G. Sha, K. Lu, Grain boundary stability governs hardening and softening in extremely fine nanograined metals. *Science* **355**, 1292–1296 (2017). <https://doi.org/10.1126/science.aal5166>
74. O. Renk, V. Maier-Kiener, I. Issa, J.H. Li, D. Kiener, R. Pippan, Anneal hardening and elevated temperature strain rate sensitivity of nanostructured metals: Their relation to intergranular dislocation accommodation. *Acta Mater.* **165**, 409–419 (2019). <https://doi.org/10.1016/j.actamat.2018.12.002>
75. X. Huang, N. Hansen, N. Tsuji, Hardening by annealing and softening by deformation in nanostructured metals. *Science* **312**, 249–251 (2006). <https://doi.org/10.1126/science.1124268>
76. A. Hasnaoui, H. Van Swygenhoven, P.M. Derlet, On non-equilibrium grain boundaries and their effect on thermal and mechanical behaviour: A molecular dynamics computer simulation. *Acta Mater.* **50**, 3927–3939 (2002). [https://doi.org/10.1016/S1359-6454\(02\)00195-7](https://doi.org/10.1016/S1359-6454(02)00195-7)
77. N.Q. Vo, J. Schäfer, R.S. Averback, K. Albe, Y. Ashkenazy, P. Bellon, Reaching theoretical strengths in nanocrystalline Cu by grain boundary doping. *Scr. Mater.* **65**, 660–663 (2011). <https://doi.org/10.1016/J.SCRIPTAMAT.2011.06.048>
78. Q. Li, J. Wang, H. Wang, X. Zhang, Achieving strong and stable nanocrystalline Al alloys through compositional design. *J. Mater. Res.* **2021**, 1–25 (2021). <https://doi.org/10.1557/S43578-021-00363-7>
79. O. Renk, A. Hohenwarter, K. Eder, K.S. Kormout, J.M. Cairney, R. Pippan, Increasing the strength of nanocrystalline steels by annealing: Is segregation necessary? *Scr. Mater.* **95**, 27–30 (2015). <https://doi.org/10.1016/J.SCRIPTAMAT.2014.09.023>
80. A.E. Perrin, C.A. Schuh, Stabilized nanocrystalline alloys: The intersection of grain boundary segregation with processing science. *Annu. Rev. Mater. Res.* **51**, 241–268 (2021). <https://doi.org/10.1146/ANNUREV-MATSCI-080819-121823>
81. Y.H. Gao, L.F. Cao, J. Kuang, H. Song, G. Liu, J.Y. Zhang, J. Sun, Solute repositioning to tune the multiple microalloying effects in an Al–Cu alloy with minor Sc, Fe and Si addition. *Mater. Sci. Eng.: A* **803**, 140509 (2021). <https://doi.org/10.1016/j.msea.2020.140509>
82. D.W. Hoffman, Perspective on stresses in magnetron-sputtered thin films. *J. Vac. Sci. Technol., A: Vac. Surf. Films* **12**, 953 (1998). <https://doi.org/10.1116/1.579073>
83. I.G. McDonald, W.M. Moehlenkamp, D. Arola, J. Wang, Residual stresses in Cu/Ni multilayer thin films measured using the Sin²ψ method. *Exp. Mech.* **59**, 111–120 (2019). <https://doi.org/10.1007/s11340-018-00447-2>
84. S. Suresh, A.E. Giannakopoulos, A new method for estimating residual stresses by instrumented sharp indentation. *Acta Mater.* **46**, 5755–5767 (1998). [https://doi.org/10.1016/S1359-6454\(98\)00226-2](https://doi.org/10.1016/S1359-6454(98)00226-2)
85. T.Y. Tsui, W.C. Oliver, G.M. Pharr, Influences of stress on the measurement of mechanical properties using nanoindentation: Part I. Experimental studies in an aluminum alloy. *J. Mater. Res.* **11**, 752–759 (1996). <https://doi.org/10.1557/JMR.1996.0091>
86. A. Bolshakov, W.C. Oliver, G.M. Pharr, Influences of stress on the measurement of mechanical properties using nanoindentation: Part II. Finite element simulations. *J. Mater. Res.* **11**, 760–768 (1996). <https://doi.org/10.1557/JMR.1996.0092>
87. K. Hono, Y. Zhang, A.P. Tsai, A. Inoue, T. Sakurai, Solute partitioning in partially crystallized Al–Ni–Ce(–Cu) metallic glasses. *Scr. Metall. Mater.* **32**, 191–196 (1995). [https://doi.org/10.1016/S0956-716X\(99\)80035-1](https://doi.org/10.1016/S0956-716X(99)80035-1)
88. S. Ruan, C.A. Schuh, Electrodeposited Al–Mn alloys with microcrystalline, nanocrystalline, amorphous and nano-quasicrystalline structures. *Acta Mater.* **57**, 3810–3822 (2009). <https://doi.org/10.1016/J.ACTAMAT.2009.04.030>
89. N.A. Belov, E.S. Naumova, Prospects for designing structural cast eutectic alloys on Al–Ce–Ni system base. *Metally (Moscow)*, pp. 146–152 (1996)
90. H. Wang, Z. Li, Z. Chen, B. Yang, Thermodynamic optimization of the Ni–Al–Ce ternary system. *J. Phase Equilib. Diffus.* **37**, 222–228 (2016). <https://doi.org/10.1007/s11669-015-0447-6>
91. A. Hasnaoui, H. Van Swygenhoven, P.M. Derlet, Cooperative processes during plastic deformation in nanocrystalline fcc metals: A molecular dynamics simulation. *Phys. Rev. B* **66**, 184112 (2002). <https://doi.org/10.1103/PhysRevB.66.184112>
92. A. Khalajhedayati, T.J. Rupert, Emergence of localized plasticity and failure through shear banding during microcompression of

- a nanocrystalline alloy. *Acta Mater.* **65**, 326–337 (2014). <https://doi.org/10.1016/j.actamat.2013.10.074>
93. T. Brink, K. Albe, From metallic glasses to nanocrystals: Molecular dynamics simulations on the crossover from glass-like to grain-boundary-mediated deformation behaviour. *Acta Mater.* **156**, 205–214 (2018). <https://doi.org/10.1016/j.actamat.2018.06.036>
94. R.W. Cheary, A. Coelho, A fundamental parameters approach to X-ray line-profile fitting. *J. Appl. Crystallogr.* **25**, 109–121 (1992). <https://doi.org/10.1107/S0021889891010804>
95. A.L. Patterson, The Scherrer formula for X-ray particle size determination. *Phys. Rev.* **56**, 978 (1939). <https://doi.org/10.1103/PhysRev.56.978>
96. C. Noyan, T.C. Huang, B.R. York, Residual stress/strain analysis in thin films by X-ray diffraction. *Crit. Rev. Solid State Mater. Sci.* **20**, 125 (1995). <https://doi.org/10.1080/10408439508243733>
97. T. Lei, J. Shin, D.S. Gianola, T.J. Rupert, Bulk nanocrystalline Al alloys with hierarchical reinforcement structures via grain boundary segregation and complexion formation. *Acta Mater.* **221**, 117394 (2021). <https://doi.org/10.1016/j.actamat.2021.117394>

Springer Nature or its licensor holds exclusive rights to this article under a publishing agreement with the author(s) or other rightsholder(s); author self-archiving of the accepted manuscript version of this article is solely governed by the terms of such publishing agreement and applicable law.